Journal of Materials Chemistry A

ROYAL SOCIETY OF CHEMISTRY

PAPER

View Article Online
View Journal | View Issue

Check for updates

Cite this: J. Mater. Chem. A, 2025, 13, 29183

Delineating the impact of Ti/Mg substitution in P2-type $Na_{2/3}Ni_{1/3}Mn_{2/3}O_2$ with an advanced electrolyte for sodium-ion batteries†

Joe Darga and Arumugam Manthiram

Received 3rd May 2025
Accepted 22nd July 2025

DOI: 10.1039/d5ta03522h

rsc.li/materials-a

Sodium layered oxide cathodes are drawing interest globally as a potential alternative to lithium layered oxides, but they suffer from egregious capacity fade and have intrinsically lower capacity. P2-type $Na_{2/3}Ni_{1/3}Mn_{2/3}O_2$ is a particularly relevant cathode material as it demonstrates an energy density of up to 550 W h kg^{-1} at high operating potentials, although this can only be maintained for a handful of cycles with industrial electrolytes. Here, a localized saturated electrolyte (LSE) is shown to significantly improve the cycle life of $Na_{2/3}Ni_{1/3}Mn_{2/3}O_2$ by suppressing the surface reactivity, despite large volume changes during cycling. The demonstrated influence of surface stability on cycle life in this work challenges the prevailing notion of a popular capacity stabilization strategy with titanium/magnesium co-doping, which is primarily thought to improve cycle life *via* improved structural stability. Single crystals of $Na_{2/3}Ni_{1/3-x}Mg_xMn_{2/3-2x}Ti_{2x}O_2$ (x = 0, 1/48, 1/24, 1/12) materials are cycled with a traditional electrolyte and the LSE to demonstrate that despite eliminating the phase transition with dopants in $Na_{2/3}Ni_{1/4}Mg_{1/12}Mn_{1/2}Ti_{1/6}O_2$, the predominant role of the dopants is in reducing the parasitic oxygen reactivity at the cathode surface. The different roles these dopants play are systematically disambiguated, and this work can guide future research to focus on reducing the parasitic cathode/electrolyte reactivity further.

Introduction

Sodium-ion batteries (SIBs) employing intercalation-based cathodes are appealing for alleviating the geopolitical and supply chain issues associated with current lithium-based cathode materials as sodium is ubiquitously distributed compared to global lithium reserves, which are primarily concentrated in four major countries, and can utilize more abundant transition metals.[1] Sodium layered oxides are promising cathode candidates for industrialization due to the similarities shared with the analogous lithium layered oxide materials that are produced at an industrial scale globally.[2–4] Rechargeable batteries are being increasingly used for portable energy storage, such as cell phones, electric vehicles, and even unmanned drones. This demand is expected to surge in the coming decades and technological innovation that can utilize more abundant materials will be pivotal to meeting the demand for energy storage.[5]

Compared to industrially relevant lithium layered oxide chemistries, sodium layered oxides typically suffer from lower practical capacity. Part of this issue is inherent as theoretical capacity is lower due to utilizing a heavier alkali ion as the working ion within the material (~275 mA h g^{-1} for $LiMO_2$ compared to ~240 mA h g^{-1} for $NaMO_2$), although it does not fully account for the differences. As a consequence of the larger ionic size of Na^+, cycling to higher states of charge typically results in larger volumetric expansion, which cascades into a collapse of the crystal lattice and ionic isolation of the active material.[6–8] To improve cycling, the oxidative voltage limit is typically limited to ~4 V *vs.* Na/Na^+ (4.3 *vs.* Li/Li+), but this in turn limits the capacity significantly. Under these conditions, P2-type $Na_{2/3}Ni_{1/3}Mn_{2/3}O_2$ (NM12) is a popular material for its electrochemical stability as it can achieve over 1000 cycles at 1C rate with 80 mA h g^{-1} capacity.[9–11] This corresponds to roughly only half of the accessible capacity from the material, as increasing the upper cut-off voltage to 4.5 V *vs.* Na/Na^+ achieves 150 mA h g^{-1} discharge capacity in the initial cycles. The "P2" type is named in accordance with Delmas notation where the letter indicates the site occupation for the Na+ ion within the phase (P for trigonal prismatic, O for octahedral) and the number indicates the number of transition metal layers in each unit cell.[12]

Cycling NM12 above 4.1 V causes the material to undergo a P2–O2 phase transition that corresponds to a >20% volumetric contraction.[13] This transition is highly unstable and as a result, capacity typically falls below 80% retention within 10 cycles or less with a 4.5 V upper cut-off.[14] The high voltage cycling must be stabilized to improve the energy density of SIBs.[15]

Materials Science and Engineering Program and Texas Materials Institute, The University of Texas at Austin, Austin, Texas 78712, USA. E-mail: manth@austin.utexas.edu

† Electronic supplementary information (ESI) available. See DOI: https://doi.org/10.1039/d5ta03522h

Traditionally, dopants have been used to help avoid the formation of the O2 phase, the most common and abundant of which being titanium and magnesium. In $Na_{2/3}Ni_{1/3}Mn_{1/2}Ti_{1/6}O_2$, the OP4 phase (an intergrowth with alternate stacking of O2 and P2 layers) can be observed, which reduces anisotropic strain and improves cycle life.[6,16] *Operando* XRD techniques have been used extensively to investigate the structural evolution of P2-type materials as sodium is extracted.[14–18] Mg is electrochemically inactive as a dopant and functions as a pillaring ion, which has also been shown to prevent the layers from fully collapsing into the O2 phase.[19–22] Co-doping with Ti and Mg can eliminate the formation of the O2 phase altogether, maintaining the hexagonal P2 phase during cycling up to 4.5 V *vs.* Na/Na^+ as sodium is extracted *via* a solid-solution mechanism.[14,22,23] Specifically, Komaba's group has recently investigated the structural evolution of a series of $Na_{2/3}[Ni_{1/4}Mn_{1/2}Ti_{1/6}X_{1/12}]O_2$ materials for the influence of the co-dopant X. When comparing X = Ti, Mg, Cu, and Zn, they demonstrated that Mg, Cu, and Zn can all suppress the formation of the O2 phase, while Zn and Cu can also effectively prevent Na^+-vacancy ordering. However, we believe that the pure structural argument regarding the influence dopants have on capacity retention is incomplete.[14]

While these dopants are effective at mitigating capacity loss over cycling, it comes at the cost of a significant proportion of the available capacity. Compared to the 150 mA h g^{-1} achieved at 4.5 V with $Na_{2/3}Ni_{1/3}Mn_{2/3}O_2$, $Na_{2/3}Ni_{1/4}Mg_{1/12}Mn_{1/2}Ti_{1/6}O_2$ can only achieve ~115 mA h g^{-1}, a reduction of about 25%. Additionally, other fundamental changes, such as alterations to the cathode particle morphology with single-crystal materials, have been shown to improve the capacity retention of sodium layered oxides without sacrificing the capacity.[11,24,25] It is important to note that our use of the term "single crystal" is only consistent with battery literature, where it is used more loosely to refer to large, isolated primary particles. The main motivation is to minimize the secondary structure formed during synthesis, and the large primary particles may or may not have several crystal domains.[25]

Single-crystal materials have been shown to be beneficial to suppressing capacity loss occurring due to intergranular particle cracking and dissolution at grain boundaries.[11,25–29] Our previous report exhibited an increase in cycle life from only 12 cycles with polycrystalline $Na_{2/3}Ni_{1/3}Mn_{2/3}O_2$ to 20 cycles with single crystal materials at an upper cut-off of 4.35 V *vs.* Na/Na^+.[11] Similarly, the detriment of the P2–O2 phase transition was shown to be overstated by employing a novel class of advanced electrolytes termed as "localized saturated electrolytes" (LSEs). More in-depth characterization of this class of electrolytes and discussion of the stabilizing mechanism is included in our previous work, including Fourier-transform infra-red spectroscopy (FTIR), synchrotron total X-ray scattering and small-angle X-ray scattering, and density functional theory (DFT) calculations.[11,30–33] In short, an inner solvation shell is created in the electrolyte around the salt ion with a saturated carbonate electrolyte, which is then solvated by a larger diluent molecule that remains inert throughout cycling. Increasing the coordination of the propylene carbonate molecules effectively raises the lowest unoccupied molecular orbital (LUMO) of the solvent–ion pair and reduces solvent oxidation at high voltages. Our report showcasing LSEs for SIBs is presently the only work covering this class of electrolytes with NaPF6 salt. There are sparse reports covering a more popular class of electrolyte termed localized high concentration electrolytes (LHCEs) that employ sodium (bis)fluorosulfonylimide (NaFSI) salt with layered oxide cathodes, with even fewer reports pursuing an aggressive voltage cut-off of 4.5 V.[34–37]

Mitigating chemical instabilities related to oxygen reactivity at high voltages by employing the LSE with single-crystal NM12 demonstrated an improvement in cycle life from 20 cycles with the 1 M $NaPF_6$ in propylene carbonate/fluoroethylene carbonate (PC/FEC, 97 : 3 by weight) electrolyte up to 50 cycles with the LSE, without sacrificing the capacity that would be required for achieving that extent of capacity retention with Ti/Mg substitution.[11]

The stability observed with the LSE and undoped NM12 was somewhat surprising given the unstable nature of the P2–O2 phase transition. With this finding, using the LSE as a more stable electrolyte offers an interesting opportunity to challenge the prevailing notion that Ti/Mg dopants primarily stabilize capacity fade by reducing the anisotropic volume change at high operating potentials. The work presented here will continue to advance the debate on whether chemical instabilities (surface) or structural instabilities (bulk) are the dominant degradation mechanism in layered oxide cathodes by systematically addressing the role of key dopants.[38]

Herein, we report single-crystal materials for four different compositions with varied Ti and Mg concentrations: $Na_{2/3}Ni_{1/3-x}Mg_xMn_{2/3-2x}Ti_{2x}O_2$ (x = 0, 1/48, 1/24, 1/12), where the morphology of isolated primary particles can be used to exclude the influence of the secondary structure on capacity fade. By examining an increasing concentration of Ti/Mg, the P2–O2 transition can be systematically suppressed, compared to a more recent work that focused on materials that fully eliminated the phase transition. All four single-crystal materials are cycled with both a baseline (1 M $NaClO_4$ in 97 : 3 PC/FEC by weight) electrolyte and an LSE. Cycling with the LSE will serve to control parasitic surface reactivity, and the varied concentration of Ti/Mg will allow for a more systematic assessment of capacity loss due to the varying extent of structural transformations. This will show that the stabilizing effect Ti/Mg co-doping is primarily through surface stabilization by reducing parasitic reactions with lattice oxygen. Pursuing this methodology allows for a more fundamental understanding of the primary function of the dopants and aims to improve the available stable capacity from sodium cathodes by reducing the need for larger quantities of dopants.

Experimental

Synthesis of single-crystal materials

For the baseline $Na_{2/3}Ni_{1/3}Mn_{2/3}O_2$ material, 1.150 g of NiO (99% purity, Sigma-Aldrich) and 2.430 g of Mn_2O_3 (99% purity, Sigma-Aldrich) powders were mixed with a mortar and pestle. 4.202 g of NaCl was then added at a ratio of 2.5 mol of NaCl

per mol of mixed NiO/Mn_2O_3 powder, with this ratio having been determined in our previous work,[11] and the mixed powder and salt were placed inside of an alumina crucible. 1.701 mL of 50% NaOH solution (99.5%, MilliporeSigma) was then added to the crucible with 5% excess NaOH to account for volatilization. The crucible was heated inside a box furnace under ambient conditions with an initial ramp rate of 5 °C min^{-1} up to 500 °C, where the temperature was held for 2 h to allow for homogeneous melting of NaOH. The furnace was then heated to 900 °C at a lower ramp rate of 1 °C min^{-1}, with a subsequent hold at 900 °C for 20 h. The furnace was then cooled down to 700 °C at a rate of 1 °C min^{-1} to allow for controlled recrystallization of any remaining NaCl, then the furnace was switched off and the material was removed once the temperature was below 200 °C. After removing from the furnace, the material was washed with water and ethanol to quickly remove any remaining NaCl. The material was then dried for 1 h at 100 °C under vacuum and stored in either a 110 °C oven or inside an argon-filled glovebox.

For the $Na_{2/3}Ni_{5/16}Mg_{1/48}Mn_{5/8}Ti_{1/24}O_2$ ($x = 1/48$) material, 1.007 g of NiO, 0.052 g of $Mg(OH)_2$ (dried, 99% purity), 2.113 g of Mn_2O_3, and 0.144 g of TiO_2 (nanosized, 99% purity) were mixed together thoroughly with a mortar and pestle with 3.88 g of NaCl and 1.582 mL of 50% NaOH solution. For the $Na_{2/3}Ni_{7/24}Mg_{1/24}Mn_{7/12}Ti_{1/12}O_2$ ($x = 1/24$) material, 1.007 g of NiO, 0.112 g of $Mg(OH)_2$, 2.118 g of Mn_2O_3, and 0.306 g of TiO_2 were mixed together thoroughly with a mortar and pestle with 4.12 g of NaCl and 1.695 mL of 50% NaOH solution. Lastly, for the $Na_{2/3}Ni_{1/4}Mg_{1/12}Mn_{1/2}Ti_{1/6}O_2$ ($x = 1/12$) material, 1.005 g of NiO, 0.262 g of $Mg(OH)_2$, 2.124 g of Mn_2O_3, and 0.716 g of TiO_2 were mixed together thoroughly with a mortar and pestle with 4.47 g of NaCl and 1.983 mL of 50% NaOH solution. The heating conditions were the same as described for the baseline material.

Electrochemical characterization

To prepare cathode composites, a ratio of active material : carbon (Super P) : polyvinylidene fluoride (PVDF) binder = 92 : 5 : 3 by weight was used. Super P carbon was premixed with half of the total desired amount of *N*-methyl-2-pyrrolidone (NMP) dispersant and mixed with a Thinky centrifugal mixer at 1000 rpm for 3 minutes. The active material was then added to the NMP/Super P mixture suspended in *N*-methyl-2-pyrrolidone (NMP) and mixed for 5 minutes at 2000 rpm. Cathode slurries were then blade-cast onto carbon-coated Al foil sheets with ~2 mg cm^{-2} active material loading. The sheets were dried at 110 °C for 15 minutes and calendared with hot rollers at 80 °C to roughly 35% porosity.

For half-cells, sodium-metal anodes were prepared (inside an argon-filled glovebox) by removing impurities with a razor blade, and then rolling and punching the metal into 1/2-inch disks. Half-cells were assembled within an argon-filled glovebox into CR2032 coin cells with glass fiber separators and 50 μL of electrolyte. 1 M $NaClO_4$ in 97 wt% propylene carbonate and 3 wt% fluoroethylene carbonate (FEC) was used as the baseline electrolyte. The LSE was made by first mixing 2.2 M concentrated $NaPF_6$ in propylene carbonate/FEC (97/3 by weight) and then adding an equal part by volume of 1,1,2,2-tetrafluoroethyl-2,2,3,3-tetrafluoropropylether (TTE) (Synquest, purity 99%) to the carbonate solution. For 2 mL of electrolyte, this corresponded to 0.3732 g $NaPF_6$ (99% purity, Sigma-Aldrich) mixed in 974.3 μL of propylene carbonate (99% purity, Sigma-Aldrich) and 25.7 μL of FEC (99% purity, Gotion). This 1 mL of solution was then mixed with 1 mL of TTE. Cells were charged at a rate of C/5 and discharged at C/3 ($C = 140$ mA g^{-1}) from 2.5 to 4.5 V for extended cycling.

For full cells, the hard carbon anodes (MTI) had a loading of 2 mA h cm^{-2}. Hard carbon anodes were presodiated within Swagelok cell cases against Na metal with the LSE and electrodes (5/8 in.) and were discharged at C/5 down to 150 mV against Na/Na^+, corresponding to ~350 mV at rest. Full cells were assembled in Hohsen CR2032 cell casings against pristine cathodes with glass fiber separators. Full cell cycling was performed at C/5 charge and C/3 discharge rates ($C = 140$ mA g^{-1}) within a voltage range of 1.9 to 4.15 V, corresponding to roughly 2.3–4.5 V *vs.* Na/Na^+. In the 26th cycle the lower limit was decreased to 1.8 V to gauge the effect of sodium inventory loss on the potential of the hard carbon anode. This difference accounted for less than 1 mA h g^{-1} in all materials when cycled and was therefore considered negligible.

Electrochemical impedance spectroscopy (EIS) was performed on a Biologic VMP3 potentiostat after first charging the full cells for 20 minutes at 28 mA g^{-1}. The frequency was scanned within a range of 500 kHz to 100 mHz, and this measurement was repeated after cycle numbers: 5, 10, 25, and 50.

The full cells that were used to gauge impedance growth over cycling had their initial cycles performed while obtaining GEIS measurements on a Biologic VMP3 potentiostat. Plotted voltage values are against Na/Na^+ and were therefore adjusted based on the operating potential of the hard carbon anode (~0.35 V). GEIS was performed with a direct current at a C/5 : C/3 charge/discharge rate and with C/10 : C/6 current perturbations, respectively. Spectra were collected from 100 kHz to 100 mHz, taking approximately three minutes per impedance spectrum. An equivalent-circuit model with four elements in series (R_{cell}, CPE_{pore}-R_{pore}, R_{CT}-CPE_{CT}, W) was used for fitting both the EIS spectra after cycling and the GEIS spectra. EIS spectra collected after specified cycle numbers were fit in the EC-Lab software, while GEIS spectra were fit in Python taking advantage of the available impedance.py package. Charge-transfer resistance (R_{CT}) values were collected from the data fits.

Materials characterization

To collect SEM images of cathode morphologies, a field emission Tescan Vega3 was used, and ImageJ software was used to measure particle size distribution statistics with 148 to 161 particles being measured for each condition to provide consistent distribution statistics.[39] ICP-OES analysis was conducted with an Agilent 5800 instrument. Samples were dissolved in a 1 : 1 volumetric ratio of concentrated hydrochloric and nitric acid. Four standards were prepared with appropriate ppm concentrations to allow for data interpolation with the linear fits of intensity *versus* concentration.

Powder XRD measurements were collected with a Miniflex 600 X-ray diffractometer with Cu Kα radiation at a scan rate of 2.5° min^{-1} at 2θ angles of 10° to 80°. Rietveld refinement for all associated diffraction materials was carried out with GSAS-II.[40]

Operando XRD was performed inside of a Rigaku Ultima IV X-ray diffractometer with Cu Kα (λ = 1.541740 Å) radiation. For the electrochemical cell, a beryllium window was used with a 2.5 μm thick aluminum foil (Geistnote) wrapped around the electrode-facing side of the window to minimize corrosion of the beryllium metal. Electrode processing for single-crystal materials with large aspect ratios is particularly important for probing the full extent of the electrochemical reaction, and the methodology for preparing free-standing cathode composites was discussed in detail in our previous work.[11] Free-standing electrodes were made with an active material: binder: conductive carbon (Super P) ratio of 75 : 15 : 10 and an electrode weight of ~2 mg cm^{-2}. The cells were cycled with the LSE unless otherwise stated at a constant C/20 rate from 2.5 to 4.5 V and XRD patterns were taken successively at a scan rate of 1° min^{-1} at 2θ angles of 12.5° to 22.5°. The smaller 2θ range allows for better resolution, while extracting as many incremental scans as possible, with the emphasized (002) peak being the most prominent for the four materials.

A Micromeritics Tristar II Plus 3030 was employed to collect nitrogen physisorption measurements within a relative pressure range (p/p_0) of 0.06 to 0.995.

A PHI VersaProbe4 Scanning XPS Microprobe with an Al Kα radiation source (1486.6 eV) was used to collect XPS data. Cathodes were disassembled inside an Ar-filled glovebox and a small portion was cut and loaded onto the XPS stage, which was then transferred in an air-tight transfer sample holder. Peak fitting and quantification were performed using CasaXPS.

Results and discussion

Synthesis of single-crystal $Na_{2/3}Ni_{1/3-x}Mg_xMn_{2/3-2x}Ti_{2x}O_2$ (x = 0, 1/48, 1/24, 1/12)

A direct molten-salt assisted synthesis method was previously demonstrated for NM12 in which NaCl salt was used during the calcination of the layered material with the active sodium chemical source (NaOH).[11] This process is shown to be applicable with Ti and Mg while maintaining phase purity, and is applied to the different compositions $Na_{2/3}Ni_{1/3-x}Mg_xMn_{2/3-2x}Ti_{2x}O_2$ (x = 0, 1/48, 1/24, 1/12) by adjusting the molar ratios of transition metals and incorporating the desired concentrations of titanium and magnesium dopants. Scanning electron micrographs (SEM) imaged in the back-scattered electron (BSE) mode are included as Fig. 1a–d for the different compositions. All compositions have predominately platelet morphology with hexagonal basal planes. Additionally, energy dispersive X-ray scattering (EDX) maps of Ni, Mn, and Ti are also included for a verification of uniform dopant incorporation with clearly increasing Ti incorporation for the increasing value of x in $Na_{2/3}Ni_{1/3-x}Mg_xMn_{2/3-2x}Ti_{2x}O_2$. The complete set of pertinent elemental maps, including Mg and Na, are included as Fig. S-1 (ESI†). The associated lattice parameters and X-ray diffraction (XRD) refinements for the four materials are included as Fig. 1f. Pertinent structural parameters obtained from refinement are included in Table S-1,† where increasing the Ti/Mg concentration gradually increases the Me–Me bond distance (a-parameter) by 0.5% with negligible changes to the c-parameter. All materials show roughly similar amounts of NiO impurities.

There have been reports in the lithium literature that titanium incorporation can serve to limit particle growth in single-crystal lithium layered oxides;[41] however, Fig. 1e shows almost no variability in the co-doped materials (2.26 μm on average), which are all marginally larger than undoped NM12 (1.89 μm). This can likely be attributed to the already rapid growth mechanism observed for the P2-type phase in undoped NM12 during synthesis, though a broader treatment of the effect of dopants on single crystal growth for sodium layered oxides is needed and can provide an interesting direction for optimizing cathode material morphology once other degradation mechanisms are reined in. Comparison of the cumulative distributions for particle size demonstrates that the three doped materials have effectively the same distribution, so particle size differences may not contribute to the differences in the electrochemistry of the materials (Fig. S-2a†). The surface area of the different materials was measured with the Brunauer–Emmett–Teller (BET) method and the nitrogen physisorption profiles (Fig. S-2b†) show a modest variation, ranging from 0.917 m^2 g^{-1} for $Na_{2/3}Ni_{1/4}Mg_{1/12}Mn_{1/2}Ti_{1/6}O_2$ to 1.367 m^2 g^{-1} for NM12.

Precise elemental ratios were measured with inductively coupled plasma optical emission spectroscopy (ICP-OES) as follows: NM12 = $Na_{0.653}Ni_{0.304}Mg_{0.002}Mn_{0.694}O_2$, T24M48 = $Na_{0.673}Ni_{0.301}Mg_{0.018}Mn_{0.639}Ti_{0.043}O_2$, T12M24 = $Na_{0.686}Ni_{0.278}Mg_{0.033}Mn_{0.604}Ti_{0.085}O_2$, and T6M12 = $Na_{0.690}Ni_{0.252}Mg_{0.077}Mn_{0.502}Ti_{0.170}O_2$, which indicate minimal deviations from the desired compositions. The intended ratios are used for clarity in the context of varied dopant concentrations, and the differences between the target and observed ratios are summarized in Table S-2.†

Electrochemical performance and structural evolution characterization

Cathodes made with the single-crystal $Na_{2/3}Ni_{1/3-x}Mg_xMn_{2/3-2x}Ti_{2x}O_2$ (x = 0, 1/48, 1/24, 1/12) materials were then tested in half-cells against a Na-metal anode with either a baseline electrolyte (1 M $NaClO_4$ in 97 wt% PC : 3 wt% FEC) or a LSE with a composition of 2.2 M $NaPF_6$ in 97 wt% PC : 3 wt% FEC that is then diluted 1 : 1 by volume with 1,1,2,2-tetrafluoroethyl-2,2,3,3-tetrafluoropropylether (TTE). Cells were cycled at 2.5–4.5 V *vs.* Na/Na^+ at a C/5 charge rate and C/3 discharge rate (1C = 140 mA g^{-1}). Fig. 2a shows the cycling performance of the four single-crystal materials with the baseline electrolyte. Without doping, single-crystal NM12 can only achieve 9 cycles before falling below 80% retention with an aggressive cut-off voltage of 4.5 V. However, introducing ~6% of the total dopants into the transition-metal composition in $Na_{2/3}Ni_{5/16}Mg_{1/48}Mn_{5/8}Ti_{1/24}O_2$ (T24M48, denoted by the fractional values of the corresponding dopants) already shows a large improvement in capacity retention after 50 cycles at 77%, up from only 38% retention for the

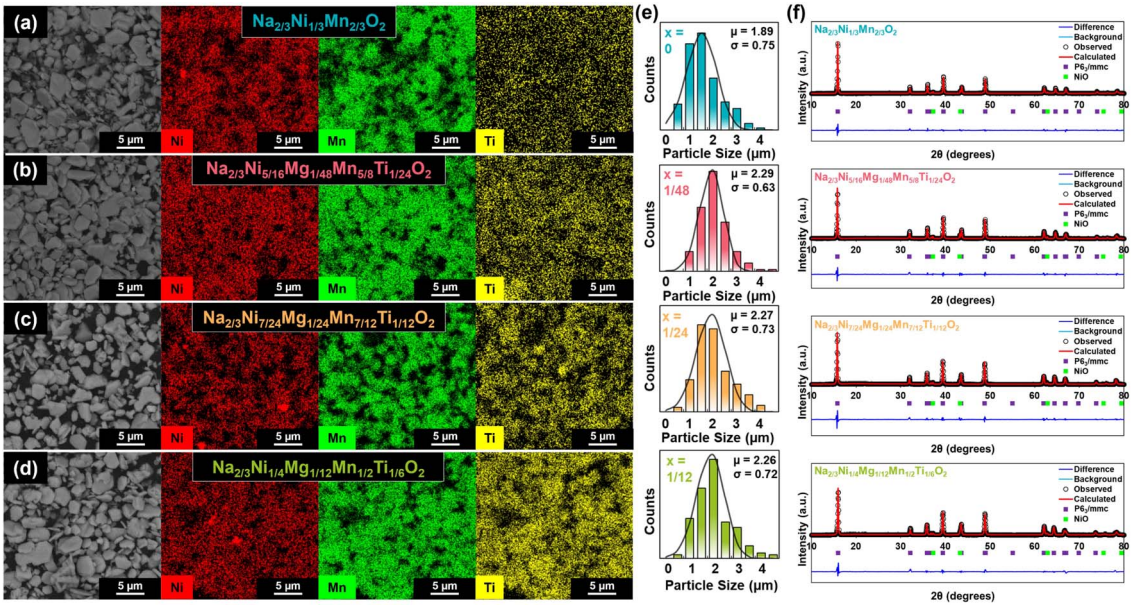

Fig. 1 (a) Backscattered-electron SEM images and Ni, Mn, and Ti EDX maps for (a) $Na_{2/3}Ni_{1/3}Mn_{2/3}O_2$, (b) $Na_{2/3}Ni_{5/16}Mg_{1/48}Mn_{5/8}Ti_{1/24}O_2$, (c) $Na_{2/3}Ni_{7/24}Mg_{1/24}Mn_{7/12}Ti_{1/12}O_2$, and (d) $Na_{2/3}Ni_{1/4}Mg_{1/12}Mn_{1/2}Ti_{1/6}O_2$. (e) Particle size distributions for the $Na_{2/3}Ni_{1/3-x}Mg_xMn_{2/3-2x}Ti_{2x}O_2$ ($x = 0$, 1/48, 1/24, 1/12) materials. (f) XRD patterns and Rietveld refinements for the single-crystal $Na_{2/3}Ni_{1/3-x}Mg_xMn_{2/3-2x}Ti_{2x}O_2$ ($x = 0$, 1/48, 1/24, 1/12) materials.

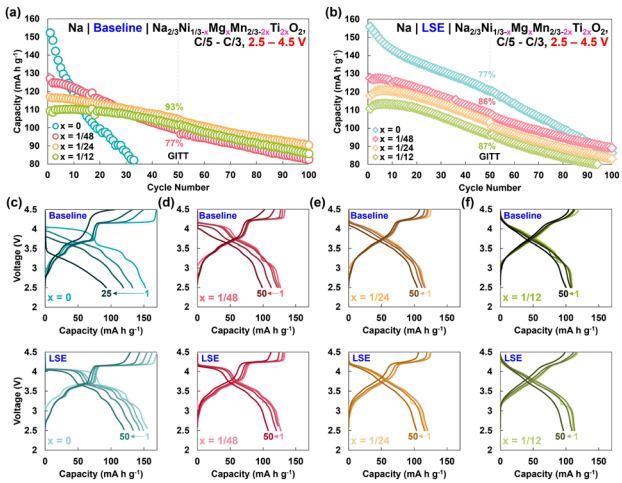

Fig. 2 (a) Cycling performances of the four different single-crystal materials in the baseline (1 M $NaClO_4$ in PC/FEC) electrolyte. (b) Cycling performances of the four different single-crystal materials in LSE electrolyte. Comparison of the voltage profiles over cycling in both electrolytes for (c) $Na_{2/3}Ni_{1/3}Mn_{2/3}O_2$, (d) $Na_{2/3}Ni_{5/16}Mg_{1/48}Mn_{5/8}Ti_{1/24}O_2$, (e) $Na_{2/3}Ni_{7/24}Mg_{1/24}Mn_{7/12}Ti_{1/12}O_2$, and (f) $Na_{2/3}Ni_{1/4}Mg_{1/12}Mn_{1/2}Ti_{1/6}O_2$.

undoped NM12 material. Even this relatively small concentration of dopants corresponds to a ~23 mA h g^{-1} loss in capacity relative to NM12. Capacity retention increases further as the concentrations of Ti and Mg in the transition-metal composition are doubled and quadrupled, with 89% retention at a ~30 mA h g^{-1} loss for $Na_{2/3}Ni_{7/24}Mg_{1/24}Mn_{7/12}Ti_{1/12}O_2$ (T12M24), and 93% retention at 50 cycles at a ~40 mA h g^{-1} loss for $Na_{2/3}Ni_{1/4}Mg_{1/12}Mn_{1/2}Ti_{1/6}O_2$ (T6M12). Capacity fade for all three doped materials is similar between 51 and 100 cycles, but there is a noticeable difference in the fade rate of T24M48 before and after performing a galvanostatic intermittent titration technique (GITT) protocol after the 50th cycle, which will be discussed later. After performing the protocol (detailed in the ESI†), some error is introduced that improves the capacity retention for T24M48 by up to 6% at 100 cycles.

Comparatively, when pairing these cathode materials with the LSE, the trend between capacity retention and dopant concentration breaks (Fig. 2b). Even at the high voltage limit of 4.5 V, undoped NM12 maintains ~77% capacity after 50 cycles, which is a substantial improvement from the same material with the baseline electrolyte. Here, $Na_{2/3}Ni_{5/16}Mg_{1/48}Mn_{5/8}Ti_{1/24}O_2$ also shows an improvement in the overall cycling performance with the LSE, maintaining 86% capacity at 50 cycles compared to only 77% with the baseline. Examining the material with the next highest Ti/Mg concentration, T12M24, does not show an additional improvement in capacity retention. T12M24 and T6M12 show nearly identical rates of capacity decay (87% at 50 cycles), which is more evident in the normalized capacity *vs.* cycling data presented in Fig. S-3.† The observed fade rate is nearly identical across all concentrations of Ti/Mg co-doped materials, which consequently means worse retention with the LSE compared to the baseline electrolyte for T12M24 and T6M12. The rate of capacity loss is similar for all three doped materials with the LSE between cycles 51 and 100, although the NM12 material suffers more fading following the GITT protocol after the 50th cycle. It is possible that the repeated rests at high voltage exasperated parasitic surface reactions, while having Ti may have protected the materials

from this interaction. In the case of T24M48 with the baseline electrolyte, it may have promoted the development of a more stable interface with the lower Ti concentration.

Fig. 2c–f compares the evolution of the voltage profiles for the four materials cycled with the baseline electrolyte and the LSE. Comparatively for NM12 and T24M48 materials, cycling with the LSE greatly improves the stability of the high-voltage phase transition, although this high voltage plateau is significantly shorter with the incorporation of Ti and Mg in T24M48. Notably for all materials with the LSE, there is an evident leftward shift of the charge profiles over continued cycling. This feature is mostly absent for any of the doped materials cycled with the baseline electrolyte, although it becomes apparent rapidly in NM12 and marginally so at the end of cycling with T24M48. The differences in the profile characteristics at high voltage warrant further exploration into how the differential capacity changes as a function of electrolyte and dopant concentration, which are included as Fig. 3a–d.

Specifically focusing on the baseline electrolyte, the high voltage $dQ\,dV^{-1}$ peak becomes rapidly unstable in the undoped NM12, showing significant degradation in the charge profile after 10 cycles. Prior to rapid degradation, the peak intensities for the lower voltage capacity (sodium vacancy reordering in the P2 phase) remain relatively constant, while the high voltage peak decreases in intensity and shifts rightward. There is an even larger shift in the voltage onset of the P2–O2 transition on discharge due to extreme polarization growth, all signs pointing to advanced degradation at the particle surface. Incrementally increasing the Ti/Mg concentration to T24M48 from undoped NM12 significantly alleviates this polarization growth and loss of accessible active sodium even when cycling with the baseline electrolyte. The high-voltage peak remains roughly at the same location on charge, though it broadens to the right, which indicates a growing kinetic hindrance to the phase transition. This effect is more pronounced on discharge, though capacity from the lower peaks remains relatively stable (discharge peaks around ~3 V for any material are Na-metal artifacts due to an overpotential in removing plated Na from charge *vs.* uncycled Na metal in the initial cycles).[11]

Further increasing the Ti/Mg content to T12M24 and T6M12 reduces the broadening of the high voltage peak during cycling and decreases the maximum peak intensity. The overall shape of the $dQ\,dV^{-1}$ profiles gradually homogenizes towards a rectangular shape consistent with a pure solid-solution reaction. Comparing successive pairs of materials based on the Ti/Mg content, the largest improvement comes from incorporating the smallest concentration of dopants in T24M48 compared to the undoped NM12 material. This suggests that the mere inclusion of Ti and Mg offers the largest benefit, with diminishing returns as the Ti/Mg is increased. There is one particularly interesting feature of the $dQ\,dV^{-1}$ profiles present in all the materials containing Ti/Mg, which is the formation of a more pronounced peak below 2.8 V on discharge. In all cases, but especially for T6M12, the peak area is larger on discharge than charge, and it appears to originate from the peak intensity corresponding to vacancy reordering between 3 and 4 V *vs.* Na/

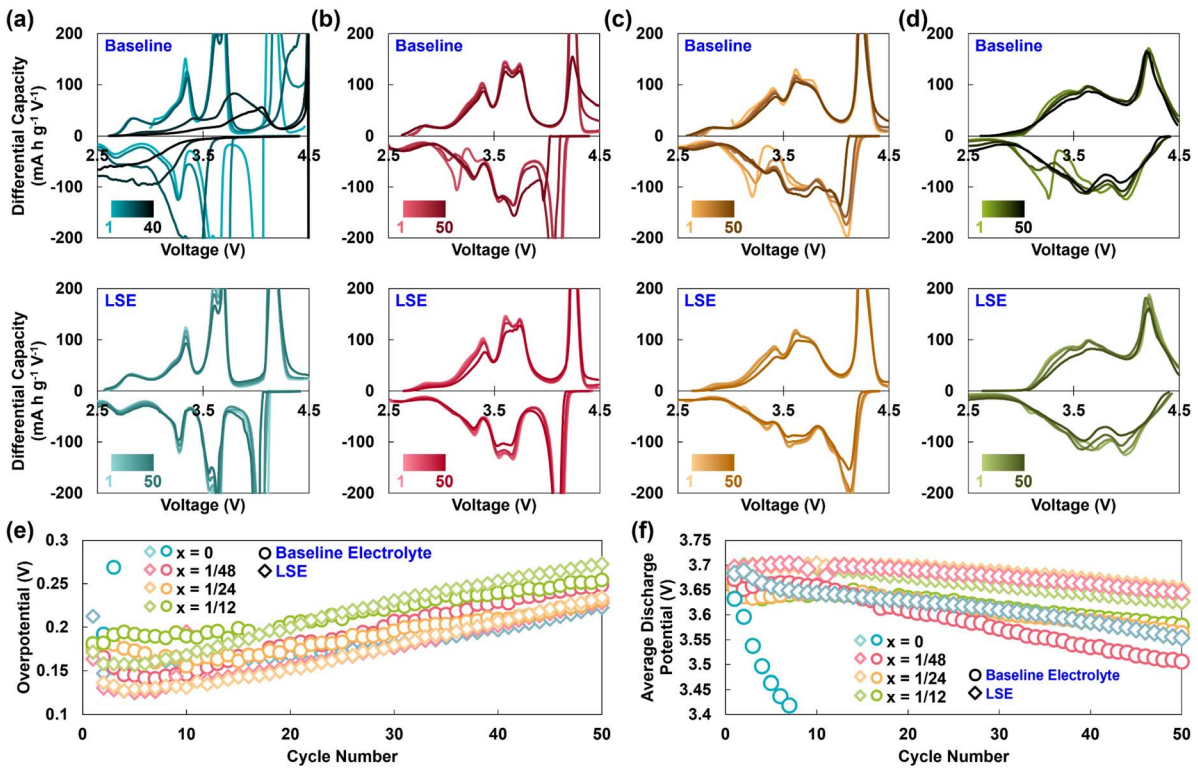

Fig. 3 Comparison of the differential capacity (mA h g^{-1} V^{-1} *vs.* V) graphs over cycling in both electrolytes for (a) $Na_{2/3}Ni_{1/3}Mn_{2/3}O_2$, (b) $Na_{2/3}Ni_{5/16}Mg_{1/48}Mn_{5/8}Ti_{1/24}O_2$, (c) $Na_{2/3}Ni_{7/24}Mg_{1/24}Mn_{7/12}Ti_{1/12}O_2$, and (d) $Na_{2/3}Ni_{1/4}Mg_{1/12}Mn_{1/2}Ti_{1/6}O_2$. (e) Overpotential growth over cycling for the four single-crystal materials in both the baseline electrolyte and LSE, and (f) the average discharge potential over cycling.

Na^+. This phenomenon and its relation to Ti/Mg has been previously demonstrated,[14] but the observation itself has not been thoroughly investigated in the literature.

Comparing the $dQ\,dV^{-1}$ plots obtained from cycling with LSE to their respective counterparts with the baseline electrolyte shows a consistent theme of reducing polarization growth and stabilizing the high voltage peak intensity over cycling with the LSE. The rightward broadening of the high voltage peak seen with the baseline electrolyte is suppressed when the same materials are cycled with the LSE, suggesting that the kinetic hindrance is alleviated by stabilizing the surface reactivity with the better electrolyte. This would indicate that increasing the Ti/Mg concentration, which demonstrates the same effect across the $dQ\,dV^{-1}$ profiles, improves the surface stability by mitigating the parasitic loss of oxygen in a manner similar to the LSE.

Notably for the profiles of all Ti/Mg containing materials cycled with the LSE, the low voltage peak intensity on discharge is greatly diminished compared to the baseline electrolyte $dQ\,dV^{-1}$ plots. In the case of T6M12 and T12M24, the poor performance of the materials when cycled with the LSE can be solely attributable to this difference. The low-voltage behaviors are more clearly visualized at the end of discharge in the voltage profiles with capacity normalized to the charge capacity achieved on each cycle (Fig. S-4†). Future research will be needed to fully explain the low-voltage phenomenon with the baseline electrolyte, employing computational modeling and synchrotron XRD, focused on the structural ordering of vacancies in the P2-phase and over extended cycling. Once this is better understood, mechanistic differences with the LSE can be further explored.

However, the low-voltage capacity being discussed accounts for relatively small values in capacity ($\sim$5 mA h g^{-1} after 50 cycles, T6M12 achieves 89 mA h g^{-1} at 3 V in both electrolytes) and does not detract from the synergistic surface stabilizing benefits of Ti/Mg incorporation and cycling with the LSE. Most importantly for the T6M12 differential capacity curves, the evolution of the peak shapes behaves similarly for both electrolytes between 3 and 4.5 V, which indicates that the stabilizing mechanisms associated with increased titanium concentration and reduced electrolyte reactivity overlap.

Overpotential and average discharge voltage over cycling are also explored to gauge the influence of surface reactivity and are plotted as Fig. 3e and f, respectively. Except for the NM12 material cycled with the baseline electrolyte and T6M12 cycled with the LSE, the overpotential is shown to be predominately dependent on the electrolyte used. In terms of average discharge potential, all three doped materials perform almost identically to the LSE despite the observed differences in voltage profiles and differential capacity. This is consistent with the observation that increasing the Ti/Mg content has the effect of "smoothing" or averaging out the peak intensity in the $dQ\,dV^{-1}$ plots over the broader voltage window as the material goes from a two-phase reaction towards a solid-solution reaction.

For cycling with the baseline electrolyte, the decrease in average discharge potential follows NM12 > T24M48 > T12M24 $\approx$ T6M12, which could be partially explained by the loss of capacity from the high-voltage region because of the deleterious phase change. However, the similarity in the degradation trends of T6M12 and T12M24 suggests that there is a surface component to the voltage decay due to a dependence of electrolyte reactivity on the Ti/Mg concentration at the particle surface, which could also explain loss of high-voltage capacity. The stark similarity in voltage decay across all three Ti/Mg containing materials when cycled in the advanced electrolyte—which offers improved surface stability—strongly supports this possibility. The difference between the average discharge voltage and overpotential stems from the evolution of the average charge potential for the LSE cycling data, which is plotted in Fig. S-5.† The average charge potential is stable for the T6M12 and T12M24 materials (after 10 cycles) with the baseline electrolyte, while the average charge potential increases for all the Ti/Mg containing materials when cycled with the LSE. This is a consequence of the loss of capacity at low voltages that is more prominent for the LSE than that for the baseline electrolyte, as discussed with the $dQ\,dV^{-1}$ profiles.

The width and magnitude of the $dQ\,dV^{-1}$ peaks, especially for the peaks above 4 V, indicate that the reaction mechanism in $Na_{2/3}Ni_{1/3-x}Mg_xMn_{2/3-2x}Ti_{2x}O_2$ gradually changes as x is increased from 0 to 1/6. To confirm this, *operando* XRD was performed on the three Ti/Mg containing materials with the LSE electrolyte, and the aggregate contour plots of successive XRD scans are included as Fig. 4a. The undoped NM12 material was demonstrated in our previous work with a well-defined P2–O2 phase transition occurring at high voltage, where the O2-phase that formed had a *c*-parameter of 8.85 Å.[11] The substitution of a small fraction, only 1/16th of the Ni/Mn for Ti/Mg in T24M48, already begins to alter this transition. A P2–OP4/O2 mixed phase transition is observed in T24M48, which is inherently noisier due to the disorder of the O2/P2 layers at the end of charge, instead of a pure P2–O2 transition. For adjacent O2 layers, the *c*-parameter is $\sim$9.1 Å, and for regions with more P2/O2 ordering (OP4 character) that value is closer to 9.6 Å. The peak positions for the (002) reflections of OP4/O2 remains relatively constant implying the two-phase reactions proceed similarly to the baseline NM12 reaction.[13]

Increasing the Ti/Mg substitution amount in $Na_{2/3}Ni_{1/3-x}Mg_xMn_{2/3-2x}Ti_{2x}O_2$ further to $x = 1/24$ (T12M24) allows for a well-ordered OP4 phase to form at high voltage with an initial *c*-parameter of 10.6 Å that gradually decreases to 10.1 Å at the end of charge as more sodium is extracted from the OP4 phase through a sodium concentration gradient. Increasing the Ti/Mg substituent amount further in $Na_{2/3}Ni_{1/3-x}Mg_xMn_{2/3-2x}Ti_{2x}O_2$ to $x = 1/12$ (T6M12) again alters the reaction mechanism at high-voltage, where a purely solid-solution reaction can be observed for the P2-phase material. Fig. 4b displays the change in the *c*-parameter of the three doped materials as a function of specific capacity. For the initial 85 mA h g^{-1} on charge, all three materials show nearly identical interlayer spacings as desodiation increases the electrostatic repulsion between oxygen layers with a < 2% change in the *c*-parameter. At this point, the *c*-parameter for T6M12 begins to decrease linearly to 94.5% of its initial value. The two-phase transition that the T12M24 material undergoes forms an OP4 phase with a smaller *c*-parameter than

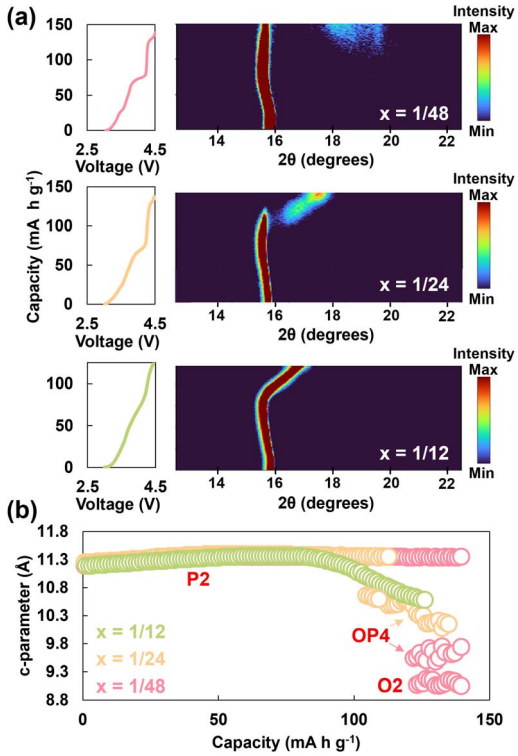

Fig. 4 (a) *Operando* XRD focused on the (002) reflection for the doped $Na_{2/3}Ni_{5/16}Mg_{1/48}Mn_{5/8}Ti_{1/24}O_2$ (x = 1/48), $Na_{2/3}Ni_{7/24}Mg_{1/24}Mn_{7/12}Ti_{1/12}O_2$ (x = 1/24), and $Na_{2/3}Ni_{1/4}Mg_{1/12}Mn_{1/2}Ti_{1/6}O_2$ (x = 1/12) materials. (b) Evolution of the c-parameter during charge for the three doped materials.

the P2-phase in T6M12 at equal capacity values and ends with an inter-layer distance that is 90.1% of its initial value. The transition for T24M48 has corresponding volume changes of roughly 86% and 81%, respectively, for the OP4 and O2 phases at 4.5 V. For a comparison, the O2 phase in NM12 has a c-parameter of 8.85 Å and 79% volumetric contraction. Each successive addition of Ti/Mg thus experiences a roughly 5% decrease in volumetric expansion compared to baseline NM12, though the electrochemical behavior does not follow this same linear pattern.

Our previous report demonstrated that there was no discernible difference in the structural evolution of NM12 when cycled with the baseline electrolyte compared to the LSE, and this holds true for T6M12 despite its poorer electrochemical performance with the LSE.[11] *Operando* XRD was performed with T6M12 and the baseline electrolyte, and the evolution of the c-parameter is compared in Fig. S-6.† Alternative visualization of the *operando* XRD data is presented for the three doped materials in Fig. S-7–S-9.† By evaluating the extreme cases of Ti/Mg doping in terms of NM12 and T6M12, this demonstrates that the LSE does not affect the structural evolution of any of the studied compositions, and the differences in the electrochemical performance when comparing the two electrolytes will be primarily due to a surface phenomenon.

Diffusion kinetics and charge transfer

Increasing the concentration of Ti and Mg in the composition of $Na_{2/3}Ni_{1/3-x}Mg_xMn_{2/3-2x}Ti_{2x}O_2$ thus has a systematic effect of shifting the electrochemical reaction from a two-phase reaction to a solid-solution reaction, with intermediate values yielding a behavior with mixed character proportional to the Ti/Mg concentration. To understand how the Ti/Mg concentration influences the diffusion kinetics, the galvanostatic intermittent titration technique (GITT) was performed on all four materials (Fig. 5). Sodium diffusion coefficients during charge were extracted from the GITT data (following the protocol described in the experimental section) and plotted against the respective state-of-charge (SOC) to allow for better cross-comparison between materials. Additionally, GITT was conducted for cells with both the baseline electrolyte and the LSE, and after 50 cycles for all conditions to gauge how the diffusion kinetics evolved depending on the Ti/Mg concentration and electrolyte choice.

Comparing only the initial cycles across the four materials, it can be seen in T24M48 that by replacing 6% of the Ni and Mn in NM12 with Mg and Ti, respectively, the Na^+ kinetics is substantially improved by 1.5 orders of magnitude above 30% SOC (from $\sim 10^{-14}$ in NM12 to 3×10^{-13} cm^2 s^{-1} in T24M48). Further increasing the concentration of Ti and Mg to T12M24 experiences a roughly one order of magnitude improvement (up to $\sim 2 \times 10^{-12}$ cm^2 s^{-1}) with double the amount of Ti and Mg, and T6M12 does not see a further improvement other than in the 30–40% SOC range where diffusion is more uniform around 10^{-12} cm^2 s^{-1} compared to that in T12M24. The kinetics for intercalation/removal of Na^+ from the P2-phase below 30% is remarkably fast and not influenced by Ti/Mg concentration. This demonstrates that there is a maximum benefit to Ti/Mg substitution in terms of improving the kinetics, and while moving towards a total solid-solution reaction like that observed in T6M12 is optimal, T12M24 or even T24M48 both offer sufficiently fast kinetics, while demonstrating predominately two-phase reactions.

In terms of understanding the degradation mechanisms of these materials as a function of the Ti/Mg concentration, a full comparison of the change in kinetics over cycling for the different electrolytes offers valuable insight. In the extreme case of undoped NM12 cycled with the baseline electrolyte, loss of active material and extreme polarization growth are both evident in the thermodynamic GITT curves and in the D_{Na^+} values, which decrease by several orders of magnitude over 50 cycles. This is only possible with severe chemical alteration to the lattice structure, or to at least the interfacial components of the particles to inhibit ion transfer. However, after 50 cycles in the LSE, the NM12 condition shows less than a 0.5 log unit decrease in the diffusion coefficient during the P2–O2 phase transition. Above 50% SOC, kinetic limitations serve to limit the charge capacity prematurely. Fig. S-10† shows the analogous graphs for the sodium diffusion coefficient on discharge *vs.* mol of Na inserted per mol of active material.

With the introduction of Ti/Mg doping in the T24M48 material, cycling with the baseline electrolyte becomes more

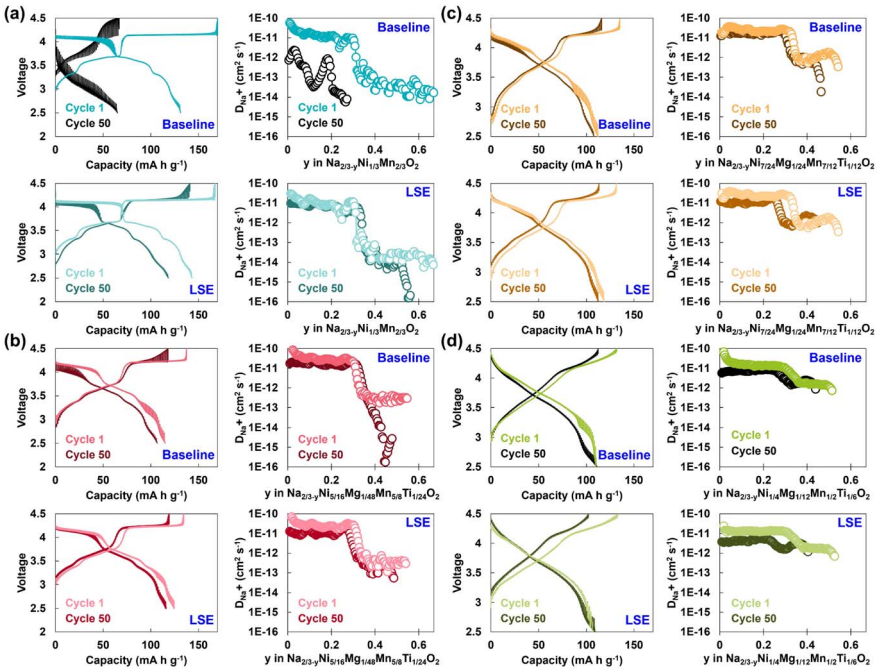

Fig. 5 Comparison of the GITT curves and calculated diffusivity coefficients *vs.* SOC, taken on the initial cycle and after 50 cycles in both electrolytes for the (a) $Na_{2/3}Ni_{1/3}Mn_{2/3}O_2$, (b) $Na_{2/3}Ni_{5/16}Mg_{1/48}Mn_{5/8}Ti_{1/24}O_2$, (c) $Na_{2/3}Ni_{7/24}Mg_{1/24}Mn_{7/12}Ti_{1/12}O_2$, and (d) $Na_{2/3}Ni_{1/4}Mg_{1/12}Mn_{1/2}Ti_{1/6}O_2$ materials.

stable in terms of isolation of active material and the kinetics at lower SOC—however, after 50 cycles, the kinetics associated with the high-voltage phase transition drops off rapidly (Fig. 5b). When the material is instead cycled 50 times with the LSE, there is negligible degradation to the sodium diffusion kinetics, though there appears to be some loss of capacity from the lower voltage region. Increasing the Ti/Mg content further to T12M24 (Fig. 5c) shows further improved stability of the high-voltage phase transition with the baseline electrolyte, though capacity is still limited by an increasing kinetic limitation at high SOC. Cycling with LSE instead again alleviates the worsening kinetics through cycling, though there is again some evidence for loss of capacity from the lower voltage region on discharge with the LSE.

Finally, an interesting pattern can be observed by comparing the changes in diffusion kinetics across the electrolytes for T6M12. First, for T6M12, the charge capacity does not become kinetically limited when cycling with the baseline electrolyte (Fig. 5d). Second, sodium diffusion kinetics at low SOC degrade more when cycled in the LSE, which holds true for all Ti/Mg containing materials. The source of this difference is more evident in the thermodynamic discharge curves after the 50th cycle for the doped materials. Specifically, across all Ti/Mg containing materials, the thermodynamic discharge curve in the 50th cycle becomes more elongated below 3 V, corresponding to the phenomenon observed in the $dQ\,dV^{-1}$ plots in Fig. 3b–d. The thermodynamic discharge curve for T6M12 shows little difference over cycling above 3 V when cycled in the LSE compared to the baseline electrolyte. Instead of a kinetic limitation on charge, the capacity loss T6M12 experiences during cycling is due to kinetic limitations on discharge (Fig. S-11†). This is further validated by the comparative discharge capacity retention during the GITT cycle after 50 cycles in each electrolyte, where the coulombic efficiencies exceed 100%. Kinetics alone does not fully explain the phenomenon for T12M24 and T24M48. However, with the observation that kinetics overall become marginally slower for materials when cycled with the LSE and the effect worsens with increasing Ti concentration, a possible reason could be the CEI components containing Ti being more insulative (as opposed to the surface reconstruction layer as a result of oxygen reactivity). Future work with time-of-flight secondary ion mass spectrometry (ToF-SIMS) and computational modeling with *ab initio* molecular dynamics may be needed to fully understand the depth profile of the CEI and its dependence on Ti concentration within the cathode. The evolution of R_{CT} over cycling is explored in the ESI† (Fig. S-12–S-14).

To further explore the roles that surface stability and titanium migration play on capacity retention, full cells were assembled with LSE and presodiated hard carbon anodes for more accurate measurements of the charge-transfer impedance compared to sodium-metal counter electrodes.

Operando galvanostatic electrochemical impedance spectroscopy (GEIS) was performed on full cells for all four materials, with impedance spectra over charge/discharge provided as Fig. 6a–d. For all materials, cathode impedance is large at low SOC, which corresponds to fully occupying available prismatic sites in the P2 phase (inserting more sodium beyond the initial amount would lead to P2–P2′ transition). The SOC onset for the R_{CT} increase has been reported in lithium-ion battery literature and is attributable to parasitic reactions at high voltage during charge.[42] At low SOC on discharge, R_{CT} increases the most for

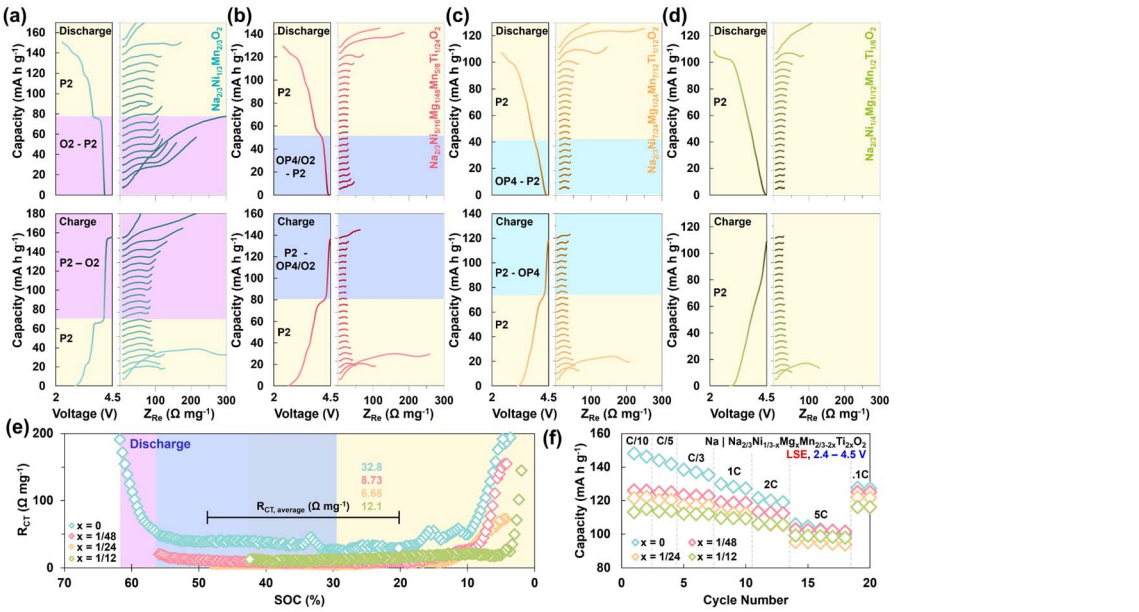

Fig. 6 *Operando* galvanostatic electrochemical impedance spectra of full cells with corresponding voltage profiles (*vs.* Na/Na^+ for reference) for (a) $Na_{2/3}Ni_{1/3}Mn_{2/3}O_2$, (b) $Na_{2/3}Ni_{5/16}Mg_{1/48}Mn_{5/8}Ti_{1/24}O_2$, (c) $Na_{2/3}Ni_{7/24}Mg_{1/24}Mn_{7/12}Ti_{1/12}O_2$, and (d) $Na_{2/3}Ni_{1/4}Mg_{1/12}Mn_{1/2}Ti_{1/6}O_2$. (e) Extracted R_{CT} values *vs.* SOC for the $Na_{2/3}Ni_{1/3-x}Mg_xMn_{2/3-2x}Ti_{2x}O_2$ materials. (f) Rate performance testing in half cells employing the LSE.

the undoped NM12 material, then T24M48, but T6M12 ruins the trend as it has higher R_{CT} than T12M24 at low SOC. Fig. S-15† shows that this increase in R_{CT} for T6M12 does not correspond to the formation of P2′, as evidenced by a comparison of the XRD peaks at OCV and after discharge down to 2.4 V *vs.* Na/Na^+.

At moderate SOC values, R_{CT} decreases for all materials and remains relatively flat from 20 to 50% SOC, and these values are used to calculate $R_{CT,average}$ (Fig. 6e). Here, all materials containing Ti/Mg have similar $R_{CT,average}$ values which are considerably smaller than that of the undoped NM12 material. The magnitude of $R_{CT,\ average}$ for the undoped NM12 material (32.8 Ω mg^{-1}) is symptomatic of excessive oxygen release and oxygen reactivity creating a resistive rock-salt phase at the surface reconstruction layer.[43,44] The difference in average charge-transfer resistances between the undoped NM12 and the doped materials (~9 Ω mg^{-1}) suggests that Ti/Mg still has a surface stabilizing effect on the CEI formation even when cycling with the LSE that has been shown to mitigate surface reactivity.

At high voltages, it becomes apparent that the R_{CT} correlates more closely with SOC than with the high-voltage transition observed. T6M12 and T12M24 do not see an increase in R_{CT} at high SOC because of thermodynamic limitations on the reversible amount of sodium that can be extracted below 4.5 V *vs.* Na/Na^+. R_{CT} increases by ~200% above $R_{CT,average}$ for T24M48 at the highest SOC, compared to ~1500% for NM12. Notably, R_{CT} begins increasing at the same SOC for both materials, but the Ti/Mg doping in T24M48 introduces a thermodynamic limitation on the SOC.

Both the charge-transfer resistance of these materials and the bulk diffusion kinetics discussed with GITT in Fig. 5 will affect the rate performance of the electrode materials when cycled with the LSE. Half-cells were thus tested at a constant C/5 charge rate up to 4.5 V with a variable discharge rate between C/10 and 5C down to 2.4 V (Fig. 6f). Undoped NM12 is the most negatively impacted at high rates due to the larger charge-transfer resistance created by oxygen reactivity at the surface and impeded bulk diffusion through the sluggish P2–O2 transition. The relatively small addition of Ti/Mg added to form T24M48 significantly improves the rate performance by improving D_{Na^+} by more than an order of magnitude at high SOC compared to NM12 and limiting R_{CT}, where T24M48 utilizes 81% of discharge capacity at 5C rate compared to only 69% for NM12. Despite another order of magnitude increase in the D_{Na^+} value at high SOC for T6M12 relative to T24M48, a marginal improvement in the relative utilization at 5C rate is seen at 85%. This marginal difference highlights the influence of charge-transfer kinetics on rate performance, as $R_{CT,average}$ is approximately equal for all the Ti/Mg containing materials. This suggests that the effect Ti/Mg has on mitigating surface reactivity is more significant for rate performance than the observed phase transition of any of the materials at high SOC and the resultant diffusion kinetics.

Surface characterization

Overall, the performance differences discussed for $Na_{2/3}Ni_{1/3-x}Mg_xMn_{2/3-2x}Ti_{2x}O_2$ ($x = 0$, 1/48, 1/24, 1/12) when cycled in the LSE and the baseline electrolyte have suggested that surface stability takes precedence over structural evolution and anisotropic strain as a mode for capacity decay.

Our previous report investigating the stabilization mechanism for a lithium-based LSE clearly demonstrated with scanning transmission electron spectroscopy and electron energy loss spectroscopy (STEM/STEM-EELS) that the formation of

surface rock-salt species was significantly suppressed when cycling at high-voltages compared to an analogous carbonate-based electrolyte. These rock-salt phases are formed through parasitic oxygen reactivity with the electrolyte.[28] To evaluate the effect of Ti concentration on the composition of the CEI, X-ray photoelectron spectroscopy (XPS) was performed on cathodes of NM12, T24M48, and T6M12 after 50 cycles with the baseline electrolyte unless otherwise stated (Fig. 7). Ti is specifically emphasized for its demonstrated effect on stabilizing the oxygen framework at the surface, while Mg serves as a synergistic co-dopant and pillaring ion.[45–47] Here, the C 1s, O 1s, and F 1s regions are emphasized, with the peaks of interest being those that correspond to possible oxygen reactivity from the cathode.

When examining the relative proportions of the peak intensity associated with C–OH and C=O bonding in the O 1s, the general trend is slightly convoluted by the relative extent of cycling for the NM12 material, which only underwent 30 cycles compared to 50 for the other materials. By 30 cycles, NM12 cycled in the baseline electrolyte has degraded to the extent that the full electrochemical reaction becomes inaccessible. Despite the shorter extent of cycling, the concentration of C–OH present in the CEI is the largest for the NM12 material, and the C=O concentration would likely be much larger than the amount present in the T24M48 CEI if the reaction were to continue out to 50 cycles. The relative ratios of the peaks observed in Fig. 7a–c are somewhat obfuscated by variability in the full width at half maximum value (FWHM) differing by ~10% because of variations in chemical environments present within the different CEIs. To more clearly emphasize the differences in composition, the calculated atomic concentrations (%) from the peak areas are provided as Fig. 8d. Here it becomes more obvious that the overall concentration of C–OH bonds in the CEI for T24M48 is smaller than that in the CEI NM12, and that the CEI on cycled T6M12 is also marginally reduced. However, there is a far more significant reduction in the C=O atomic percentage in the CEI of T6M12 when compared to T24M48. The total oxygen concentration present within the CEI for these two peaks is 31.8% for T24M48 and 24.3% for T6M12. Atomic concentrations of TM–O and Na–F bonds are provided in Fig. S-16.† The larger TM–O bonds in the NM12 sample may also indicate a thinner CEI with a higher degree of degradation. Interestingly, the concentration of Na–F is lowest for NM12 and considerably higher for T24M48 and T6M12, but for the rapid capacity decay observed in these materials the reactivity of surface oxygen will be more insightful.

The C 1s, O 1s, and F 1s XPS spectra collected from cathodes cycled 50 times with the LSE are provided as Fig. 8, and atomic percentages for the C–O and C=O peaks in the O 1s spectra are provided as Fig. S-17.† Comparing this to Fig. 7d, there is an immediate and obvious difference in that the undoped NM12 material has a substantially lower percentage of C=O bonds present in its CEI when cycled with the LSE compared to the baseline electrolyte. In fact, the percentage of C=O bonds is roughly the same for all the materials and is considerably lower when compared to the same materials cycled in the baseline electrolyte. The relative proportion of the C=O to C–OH bonds increases with increasing Ti/Mg concentration for the LSE because the C=O percentage remains relatively constant while

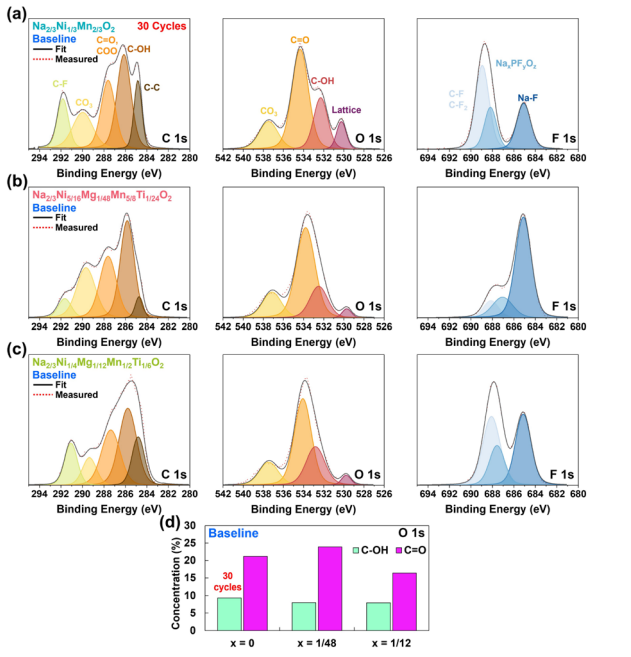

Fig. 7 Comparison of the XPS data on the C 1s, O 1s, and F 1s regions collected from cathodes after 50 cycles (unless otherwise indicated) with the baseline electrolyte for the (a) $Na_{2/3}Ni_{1/3}Mn_{2/3}O_2$, (b) $Na_{2/3}Ni_{5/16}Mg_{1/48}Mn_{5/8}Ti_{1/24}O_2$, and (c) $Na_{2/3}Ni_{1/4}Mg_{1/12}Mn_{1/2}Ti_{1/6}O_2$ materials. (d) Atomic percentage of O 1s peaks associated with C–OH and C=O bonding modes for the three different cycled cathode materials.

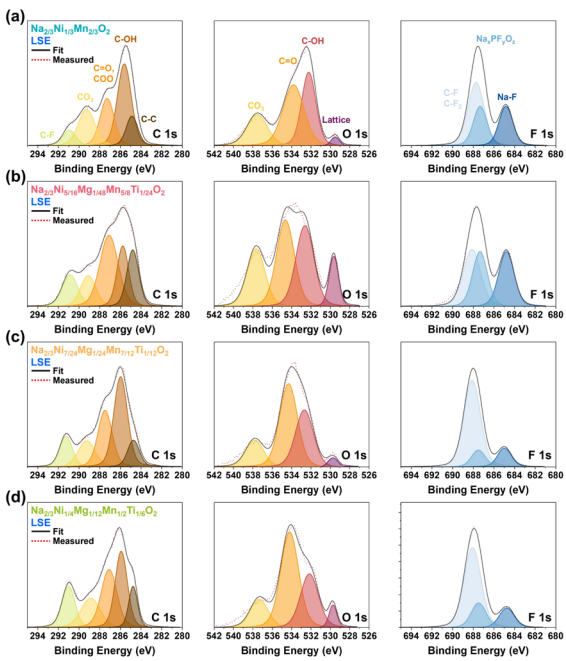

Fig. 8 Comparison of the XPS data collected on the C 1s, O 1s, and F 1s regions from cathodes after 50 cycles with the LSE for the (a) $Na_{2/3}Ni_{1/3}Mn_{2/3}O_2$, (b) $Na_{2/3}Ni_{5/16}Mg_{1/48}Mn_{5/8}Ti_{1/24}O_2$, (c) $Na_{2/3}Ni_{7/24}Mg_{1/24}Mn_{7/12}Ti_{1/12}O_2$, and (d) $Na_{2/3}Ni_{1/4}Mg_{1/12}Mn_{1/2}Ti_{1/6}O_2$ materials.

the C–OH concentration decreases. The total oxygen concentration decreases going from NM12 to T6M12 as follows: 20%, 18.5%, 18.4%, and 18%, where the largest incremental difference is seen going from NM12 to T24M48. This indicates that parasitic oxygen reactivity is substantially reduced by the LSE for all materials, and including a small amount of Ti/Mg in the composition has the largest marginal benefit on reducing oxygen reactivity, but there is still a more marginal and synergistic benefit gained by increasing the Ti/Mg concentration further. The TM-O concentration is similar for all materials cycled in the LSE, though it increases linearly with Ti/Mg concentration which may indicate a trend for reducing CEI thickness (Fig. S-16†). These findings are consistent with the overall trend in capacity retention for the Ti/Mg containing materials when cycled with the LSE.

Titanium coatings are commonly employed to alleviate parasitic surface reactions, and titanium migration has been shown to occur in other sodium layered oxides (with cross-sectional STEM-EELS) to form a pseudo-coating at the electrode surface.[43–45] A more detailed emphasis on surface speciation is provided in the literature.[45] The relative extent of titanium migration for the different Ti/Mg containing materials was explored with XPS for the Ti 2p and Mn 2p regions of pristine powders for T24M48, T12M24, and T6M12 (Fig. S18†). It was determined that larger proportions of titanium were present at the surface for the lower concentration materials, suggesting titanium migration influences the surface Ti concentration and subsequent surface reactivity.

When comparing successive samples, the largest incremental benefit on electrochemical performance comes when comparing NM12 to T24M48. T24M48 also shows the largest relative extent of Ti migration at the surface, while still undergoing a relatively large volume change at high voltage during cycling with a transition to a mixed OP4/O2 phase. The summation of these factors emphasizes the significance that the surface stabilizing effect of titanium addition has on improving the electrochemical performance of P2-type $Na_{2/3}Ni_{1/3}Mn_{2/3}O_2$, independent of the structural behavior of the materials at high voltage.

Conclusions

A novel, molten-salt assisted synthesis method involving NaCl addition during solid-state calcination was used to form single-crystal materials of the form $Na_{2/3}Ni_{1/3-x}Mg_xMn_{2/3-2x}Ti_{2x}O_2$ ($x = 0$, 1/48, 1/24, 1/12). The use of single-crystal materials in this manner controlled the capacity degradation mode of intergranular particle cracking in sodium layered oxides. Two electrolytes were used in half-cells, a standard carbonate-based electrolyte with $NaClO_4$, and a localized saturated electrolyte (LSE). Comparison of electrochemical cycling behavior for the four cathode materials with the two different electrolytes allowed for a systematic disambiguation of the competing influence titanium has as a dopant for both mitigating surface degradation and reducing anisotropic volume changes. *Operando* XRD demonstrated a systematic shift in the high-voltage phase transition towards a solid-solution reaction with minimal volume change as the value of x is increased in $Na_{2/3}Ni_{1/3-x}Mg_xMn_{2/3-2x}Ti_{2x}O_2$. Despite this, all three Ti/Mg containing materials demonstrated similar rates of capacity decay, with $Na_{2/3}Ni_{5/16}Mg_{1/48}Mn_{5/8}Ti_{1/24}O_2$ retaining 86% capacity at 50 cycles (77% with the baseline electrolyte) compared to 87% for both $Na_{2/3}Ni_{7/24}Mg_{1/24}Mn_{7/12}Ti_{1/12}O_2$ and $Na_{2/3}Ni_{1/4}Mg_{1/12}Mn_{1/2}Ti_{1/6}O_2$ when cycled with the stable LSE.

The CEI of cycled electrodes was probed with XPS for evidence of parasitic oxygen reactivity, with the CEIs of cathodes cycled with the baseline electrolyte demonstrating much larger concentrations of reacted oxygen species that decreased with Ti/Mg concentration. Variance in oxygen content across the CEIs of cathodes cycled with the LSE was minimal, with the undoped NM12 material having the largest concentration of reacted oxygen in the CEI. These factors strongly suggest that incorporation of titanium stabilizes capacity primarily by stabilizing the electrode surface. When the less reactive electrolyte was used, the difference in capacity retention was greatly reduced across the four materials as increasing the surface Ti concentration had diminishing returns in preventing surface reactions. These findings were further supported by the analysis of GEIS data during discharge that compared the charge-transfer kinetics across materials and showed a dependence on Ti/Mg incorporation, but not concentration. Post-mortem GITT further corroborated these findings by demonstrating that worsening diffusion kinetics over cycling depended primarily on the surface reactivity of the electrode/electrolyte pair, where changes to the D_{Na^+} coefficient above 3.2 V were minimal in pairings with either higher Ti/Mg in the cathode or when the materials were cycled with the LSE. This work has fundamental implications for understanding the bulk *vs.* surface debate of capacity degradation in layered oxides.

By developing a better understanding of the role dopants play, lower concentrations can be used that allow for the maximum possible discharge capacity. This work thus encourages further demystification of the competing effects of different dopants with structural and surface components—such as Zn and Al—or combinations of small quantities of many dopants in a systematic way. It similarly encourages extension to other materials with different high-voltage phase transitions besides the P2–O2 observed in NM12. It also strongly suggests that electrolyte stability will be the limiting factor for capacity retention of sodium layered oxides moving forward, and with sodium-based LSEs being in their infancy, this offers many exciting avenues for exploration into the design of this new class of electrolyte. Future work should also focus on developing an understanding of what causes the change in the low-voltage discharge behavior of the Ti/Mg containing P2-type materials after repeated cycling. Once this fundamental understanding is built, it can be used to further improve the electrolyte design to mitigate the gradual loss of capacity at low voltage with the LSE and Ti/Mg containing materials.

Author contributions

J. D. performed the experimental work and data analysis. All the authors wrote the manuscript. A. M. supervised the research.

Conflicts of interest

There are no conflicts to declare.

Acknowledgements

This work was supported by the U.S. Department of Energy, Office of Basic Energy Sciences, Division of Materials Science and Engineering under award number DE-SC0005397. The authors thank Mr Seamus Ober for his assistance with the ICP-OES measurements.

References

1 K. Sada, J. Darga and A. Manthiram, *Adv. Energy Mater.*, 2023, **13**, 2302321.
2 J. Darga, J. Lamb and A. Manthiram, *Energy Technol.*, 2020, **8**, 2000723.
3 S. Chen, C. Wu, L. Shen, C. Zhu, Y. Huang, K. Xi, J. Maier and Y. Yu, *Adv. Mater.*, 2017, **29**, 1700431.
4 S. Y. Hong, Y. Kim, Y. Park, A. Choi, N. S. Choi and K. T. Lee, *Energy Environ. Sci.*, 2013, **6**, 2067.
5 A. Manthiram, *Nat. Commun.*, 2020, **11**, 1550.
6 Z. Cheng, B. Zhao, Y. Guo, L. Yu, B. Yuan, W. Hua, Y. Yin, S. Xu, B. Xiao, X. Han, P. Wang and Y. Guo, *Adv. Energy Mater.*, 2022, **12**, 2103461.
7 H. Yoshida, N. Yabuuchi, K. Kubota, I. Ikeuchi, A. Garsuch, M. Schulz-Dobrick and S. Komaba, *Chem. Commun.*, 2014, **50**, 3677.
8 Y. Zhang, M. Wu, J. Ma, G. Wei, Y. Ling, R. Zhang and Y. Huang, *ACS Cent. Sci.*, 2020, **6**, 232.
9 X. Zheng, P. Li, H. Zhu, K. Rui, G. Zhao, J. Shu, X. Xu, W. Sun and S. X. Dou, *Energy Storage Mater.*, 2018, **15**, 257.
10 J. Zhang, W. Wang, W. Wang, S. Wang and B. Li, *ACS Appl. Mater. Interfaces*, 2019, **11**, 22051.
11 J. Darga and A. Manthiram, *Adv. Funct. Mater.*, 2024, **34**, 2408642.
12 C. Delmas, C. Fouassier and P. Hagenmuller, *Physica B+C*, 1980, **99**, 81.
13 Z. Lu and J. R. Dahn, *J. Electrochem. Soc.*, 2001, **148**, A1225.
14 K. Kubota, T. Asari and S. Komaba, *Adv. Mater.*, 2023, **35**, 2300714.
15 Z. Chen, Y. Deng, J. Kong, W. Fu, C. Liu, T. Jin and L. Jiao, *Adv. Mater.*, 2024, **36**, 2402008.
16 N. Tapia-ruiz, W. M. Dose, N. Sharma, H. Chen, J. Heath, J. W. Somerville, U. Maitra, M. S. Islam and P. G. Bruce, *Energy Environ. Sci.*, 2018, **11**, 1470.
17 K. Kubota, S. Jumakura, Y. Yoda, K. Kuroki and S. Komaba, *Adv. Energy Mater.*, 2018, **8**, 1703415.
18 J. W. Somerville, A. Sobkowiak, N. Tapia-Ruiz, J. Billaud, J. G. Lozano, R. A. House, L. C. Gallington, T. Ericsson, L. Häggström, M. R. Roberts, U. Maitra and P. G. Bruce, *Energy Environ. Sci.*, 2019, **12**, 2223.
19 Z. Hu, Y. Niu, Y. Liu, J. Zhang and X. Rong, *Nat. Energy*, 2024, **9**, 1529.
20 H. Li, P. Zhou, F. Liu, H. Li, F. Cheng and J. Chen, *Chem. Sci.*, 2019, **10**, 1374.
21 Q. Xie, W. Li and A. Manthiram, *Chem. Mater.*, 2019, **31**, 938.
22 K. Wang, H. Wan, P. Yan, X. Chen, J. Fu, Z. Liu and H. Deng, *Adv. Mater.*, 2019, **31**, 1904816.
23 Q. Mao, Y. Yu, J. Wang, L. Zheng, Z. Wang, Y. Qiu, Y. Hao and X. Liu, *J. Mater. Chem. A*, 2021, **9**, 10803.
24 J. Darga and A. Manthiram, *Adv. Funct. Mater.*, 2025, **35**, 2420706.
25 J. Langdon and A. Manthiram, *Energy Storage Mater.*, 2021, **37**, 143.
26 V. Pamidi, S. Trivedi, S. Behara, M. Fichtner and A. Reddy, *iScience*, 2022, **25**, 104205.
27 X. Kong, H. Yang, Y. Zhang, P. Dai, Y. Tang, J. Zeng and J. Zhao, *Chem. Eng. J.*, 2023, **452**, 139431.
28 P. Pang, X. Tan, Z. Wang, Z. Cai, J. Nan, Z. Xing and H. Li, *Electrochim. Acta*, 2021, **365**, 137380.
29 J. Darga and A. Manthiram, *ACS Appl. Mater. Interfaces*, 2022, **14**, 52729.
30 L. Su, E. Jo and A. Manthiram, *ACS Energy Lett.*, 2022, **7**, 2165.
31 L. Su, X. Zhao, M. Yi, H. Charalambous, H. Celio, Y. Liu and A. Manthiram, *Adv. Energy Mater.*, 2022, **12**, 2201911.
32 M. Yi, L. Su and A. Manthiram, *J. Mater. Chem. A*, 2023, **11**, 11889.
33 J. B. Adamo, L. Su and A. Manthiram, *ACS Appl. Mater. Interfaces*, 2023, **15**, 15458.
34 Y. Jin, P. M. L. Le, P. Gao, Y. Xu, B. Xiao, M. H. Engelhard, X. Cao, T. D. Vo, J. Hu, L. Zhong, B. E. Matthews, R. Yi, C. Wang, X. Li, J. Liu and J. G. Zhang, *Nat. Energy*, 2022, **7**, 718.
35 J. Zheng, S. Chen, W. Zhao, J. Song, M. H. Engelhard and J. G. Zhang, *ACS Energy Lett.*, 2018, **3**, 315.
36 J. He, A. Bhargav, L. Su, J. Lamb, J. Okasinski, W. Shin and A. Manthiram, *Nat. Energy*, 2024, **9**, 446.
37 J. Lamb and A. Manthiram, *ACS Appl. Mater. Interfaces*, 2022, **14**, 28865.
38 S. Lee, L. Su, A. Mesnier, Z. Cui and A. Manthiram, *Joule*, 2023, **7**, 2430.
39 C. A. Schneider, W. S. Rasband and W. Eliceiri, *Nat. Methods*, 2012, **9**, 671.
40 B. H. Toby and R. B. Von Dreele, *J. Appl. Crystallogr.*, 2013, **46**, 544.
41 A. Mesnier and A. Manthiram, *J. Power Sources*, 2023, **586**, 233681.
42 R. Morasch, H. A. Gasteiger and B. Suthar, *J. Electrochem. Soc.*, 2023, **170**, 080522.
43 S. Lee, K. Scanlan, S. Reed and A. Manthiram, *Adv. Energy Mater.*, 2025, **15**, 2403002.
44 F. Lin, I. M. Markus, D. Nordlund, T. C. Weng, M. D. Asta, H. L. Xin and M. M. Doeff, *Nat. Commun.*, 2014, **5**, 3529.
45 M. A. Razmjoo Khollari, M. K. Azar, M. Esmaeili, N. Malekpour, S. M. Hosseini-Hosseinabad, R. S. Moakhar, A. Dolati and S. Ramakrishna, *ACS Appl. Energy Mater.*, 2021, **4**, 5304.
46 Y. Yu, W. Kong, Q. Li, D. Ning, G. Schuck, G. Schumacher, C. Su and X. Liu, *ACS Appl. Energy Mater.*, 2020, **3**, 933.
47 S. Guo, Q. Li, P. Liu, M. Chen and H. Zhou, *Nat. Commun.*, 2017, **8**, 135.